Arch. Metall. Mater. **71** (2026), 2, 555-559

DOI: https://doi.org/10.24425/amm.2026.158840

SEONGHYUN PARK[1], JUNGMIN JEON[1], SEOK-JAE LEE[1,2], JAE-GIL JUNG[1,2*]

# EFFECT OF PB ADDITION ON THE SOLIDIFICATION MICROSTRUCTURE AND PRECIPITATION BEHAVIOR OF Al–10Si–0.4Mg–0.4Cu ALLOY FABRICATED BY HIGH-PRESSURE DIE CASTING

We studied the effect of Pb addition on the solidification microstructure and precipitation behavior of an Al–10Si–0.4Mg–0.4Cu alloy fabricated by high-pressure die casting (HPDC) using thermodynamic calculations and scanning and transmission electron microscopy analyses. Pb addition induced the formation of Pb phase along the grain boundaries of Al and Al/Si eutectic during solidification. Aging at 160°C induced the formation of spherical or needle-like Si nanoprecipitates and embedded $\beta''$ nanoprecipitates in both Pb-free and Pb-added alloys. Strong Pb segregation was observed at the interface of Si nanoprecipitates, which inhibits precipitate growth during aging. Si refinement due to Pb segregation and newly formed Pb nanoprecipitates slightly enhanced the age hardening reaction after T5 heat treatment. This study can provide insights into the strategies to control the microstructure of recycled HPDC Al alloys containing Pb.

*Keywords:* Recycled aluminum; high-pressure die casting; precipitation; transmission electron microscopy

## 1. Introduction

High-pressure die casting (HPDC) is a widely used method in the automotive and aerospace industries due to its high productivity, dimensional accuracy, and relatively low cost [1]. HPDC Al–Si alloys are particularly suitable for structural and powertrain applications due to their excellent castability and good combinations of strength and ductility [2-4]. To improve the mechanical properties of HPDC Al–Si alloys, age hardening due to nanoprecipitates is widely adopted [2-6]. The aging induces the formation of nanoscale strengthening precipitates such as Si, $\beta''$, and Q, depending on the alloy composition [2-7]. Direct aging of HPDC product (i.e., T5 temper) is a promising method to avoid blistering caused by entrapped gas and distortion during solution treatment and quenching process [5,8].

Recently, the aluminum industry has increasingly relied on recycled aluminum scrap to reduce production costs and carbon emissions [9-11]. This trend is particularly pronounced in the automotive industry, where large quantities of end-of-life vehicles are recycled. However, the use of recycled aluminum raises concerns related to the accumulation of impurities such as Fe, Zn, and Pb [12,13]. Especially, Pb contamination is usually unintentional and originates from scrapped automobiles, existing lead-containing aluminum alloys, or attachments such as solder or bearing materials [14]. Liquid Pb tends to separate from liquid Al and exists up to ~320°C during solidification [15]. Due to the very low Pb solubility in FCC Al matrix (<0.001% at 300°C), FCC Pb phase formed below the solvus temperature (~300°C) [15]. The soft and discrete Pb phase formed during solidification is reported to act as preferential crack initiation sites, thus deteriorating both ductility and fatigue resistance [16].

Despite growing interest in controlling scrap-related impurities, systematic studies on the effects of Pb on the microstructure and precipitation behavior of HPDC Al–Si–Mg–Cu alloys remain limited. Therefore, we studied the effects of Pb addition on the solidification microstructure and precipitation behavior of HPDC Al–10Si–0.4Mg–0.4Cu alloy.

## 2. Experimental

HPDC Al alloy with rod-type tensile specimen dimensions of ASTM E8 sub-size standard (gauge length: 25 mm) was provided by KONEC (Republic of Korea). The main processing parameters applied in HPDC were set as casting temperature 690°C, die temperature 200°C, final intensification pressure 75 MPa, and shot plunger speed 0.2-2.0 m/s. The chemical compositions of Pb-free and Pb-added were measured to be

[1] JEONBUK NATIONAL UNIVERSITY, DIVISION OF ADVANCED MATERIALS ENGINEERING, JEONJU 54896, REPUBLIC OF KOREA
[2] JEONBUK NATIONAL UNIVERSITY, RESEARCH CENTER FOR ADVANCED MATERIALS DEVELOPMENT, JEONJU 54896, REPUBLIC OF KOREA
* Corresponding author: jgjung@jbnu.ac.kr

Al–10.42Si–0.49Mg–0.46Cu–0.36Mn–0.19Fe–0.02Ti–0.01Sr (wt.%) and Al–10.53Si–0.47Mg–0.43Cu–0.36Mn–0.13Fe–0.02Ti–0.01Sr–0.63Pb (wt.%), respectively, using optical emission spectroscopy analysis.

The disk-shaped specimens (Φ6×4 mm), taken from the HPDC samples, were aged at 160°C for 8 h (T5 temper) and quenched into water at room temperature. The hardness of as-cast and T5 specimens was measured ten times using a Vickers hardness tester (Mitutoyo, HM-122) under a load of 0.2 kgf and dwell time of 10 s.

After the specimens for microstructure observation were mechanically polished, the microstructures were observed using an optical microscope (OM) (Nikon, EPIPHOT 200), a field emission scanning electron microscope (FE-SEM) (Carl Zeiss, SUPRA 40VP), and energy-dispersive X-ray spectroscopy (EDS). The grain structure was analyzed using electron backscattered diffraction (EBSD) installed in the SEM (HITACHI, SU-70). The EBSD data taken at ×500 magnification with a step size of 0.5 μm were analyzed using TSL OIM 8 software. The secondary phases and precipitates were examined using a transmission electron microscope (TEM, FEI, Talos F200X G2) and EDS operated at 200 kV. TEM samples were prepared by the focused ion beam (FIB) milling technique in an SEM (FEI, Helios G5).

## 3. Results and discussion

Figs. 1(a,b) show the variation in equilibrium phase fraction during equilibrium cooling and non-equilibrium Scheil cooling of the Pb-added alloy calculated using FactSage 8.4 software and the FTlite database [17]. This indicates the sequential formation of primary Mn/Fe-rich phases ($Al_3MnSi_2$, $\alpha$-Al(Fe,Mn)Si), Al/Si eutectic, and the phases ($\pi$-$Al_8FeMg_3Si_6$, $\theta$-$Al_2Cu$, and $Q$-$Al_5Cu_2Mg_8Si_6$) formed in the final stage of solidification. Liquid Pb is expected to transform into FCC-structured Pb phase below ~250°C. Fig. 1(c) shows the equilibrium phase fraction calculated using the Al matrix composition at 300°C (Al–1.42Si–0.19Mg–0.23Cu, wt.%) obtained from the Scheil cooling. This indicates that the Si phase is the main precipitate formed during T5 treatment of the HPDC alloy.

Fig. 1(d) shows the Vickers hardness of as-cast and T5 alloys with and without Pb addition. As-cast Pb-free alloy exhibits a lower hardness value (85.5±1.1 HV), compared to the Pb-added alloy (89. ±2.8 HV). The T5 heat treatment increased the Vickers hardness of both Pb-free alloy (from 85.5±1.1 to 98.3±1.4 HV) and Pb-added alloy (from 89.6±2.8 to 104.0±3.2 HV). The hardness increase due to T5 heat treatment was 12.8 HV for the Pb-free alloy and 14.4 HV for the Pb-added alloy.

Figs. 2(a,d) show the OM and EBSD inverse pole figure (IPF) images of Pb-free and Pb-added alloys. Both HPDC alloys consist of coarse dendritic Al grains and fine equiaxed Al grains, with average grain sizes of 25±14 μm and 26±13 μm, respectively. This indicates that the Pb addition did not significantly affect the grain size of the Al matrix. The Al/Si eutectic microstructure is also visible in both as-cast alloys. SEM (Fig. 2(b)) and EDS elemental mapping (Fig. 2(c)) results indicate that the Pb-free alloy contains $\alpha$-Al(Fe,Mn)Si phase (~5 μm), and script-like $\pi$-$Al_8FeMg_3Si_6$ and granular $\theta$-$Al_2Cu$ phases along

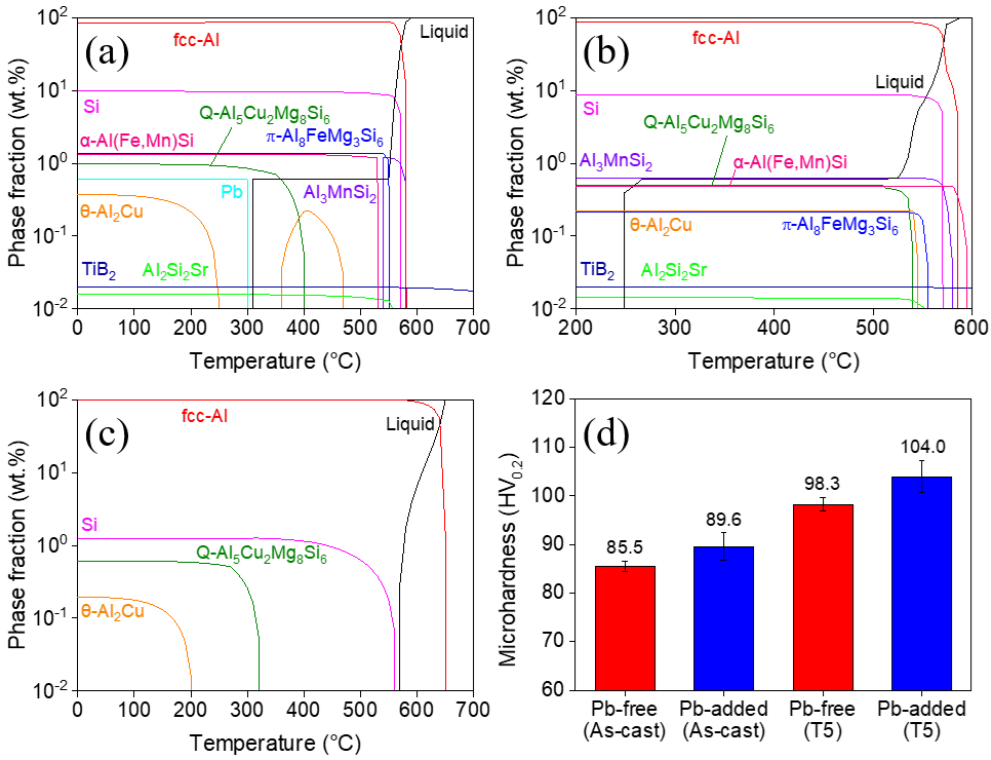


Fig. 1. Change in equilibrium phase fraction with temperature for Pb-added alloy under (a) equilibrium and (b) non-equilibrium Scheil cooling. (c) Equilibrium phase fraction with temperature for the Al matrix at 300°C in (b). (d) Vickers hardness of as-cast and T5 alloys with and without Pb addition

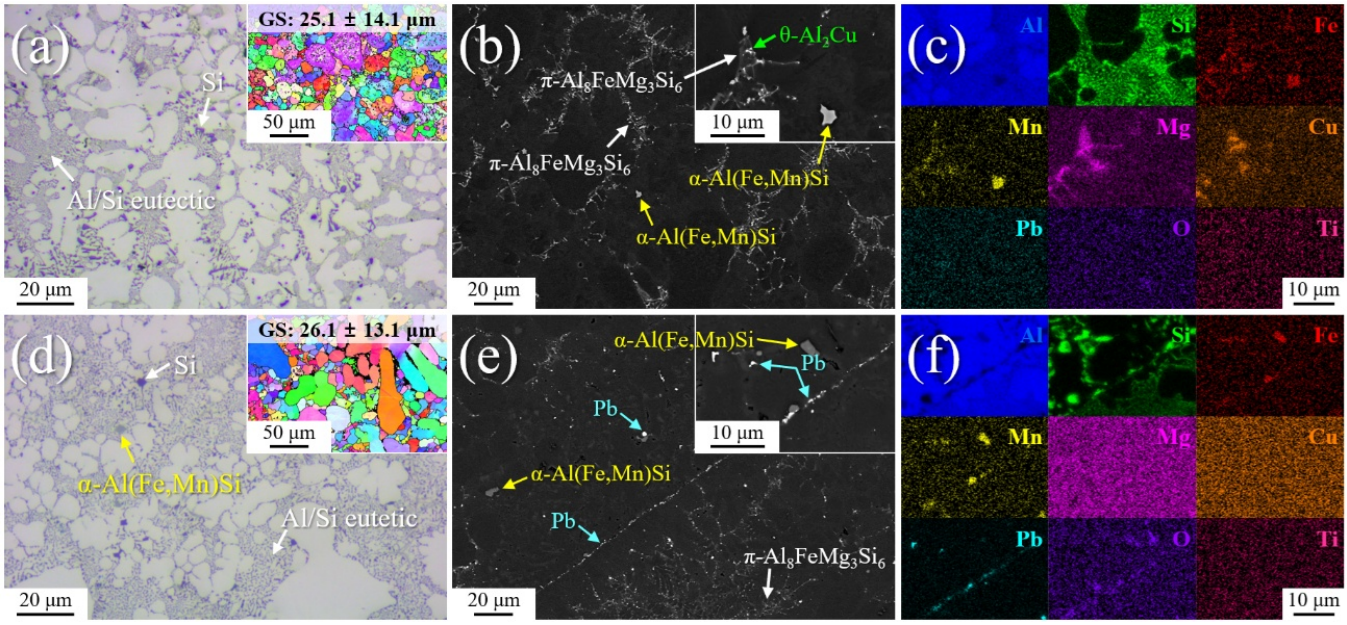


Fig. 2. (a,d) OM image (inset: EBSD IPF maps), (b,e) SEM BSE image, and (c,f) EDS element mapping of (a-c) Pb-free and (d-f) Pb-added alloy

the grain boundaries of Al/Si eutectic. Like Pb-free alloy, Pb-added alloy also contains $\alpha$-Al(Fe,Mn)Si, $\pi$-$Al_8FeMg_3Si_6$, and $\theta$-$Al_2Cu$ phases. As shown in Figs. 2(e,f), the Pb-added alloy contains additional Pb phases along the grain boundaries formed by Pb-rich liquid in the final stage of solidification.

Fig. 3(a) shows the high-angle annular dark field (HAADF) scanning TEM (STEM) image revealing α-Al(Fe,Mn)Si and eutectic Si phases of T5-treated Pb-free alloy aged at 160°C for 8 h. The $\alpha$-Al(Fe,Mn)Si phase had a Mn:Fe ratio of ~2:1 and a cubic structure ($Pm\bar{3}$; $a$ = 1.264 nm [18]) with orientation relationships

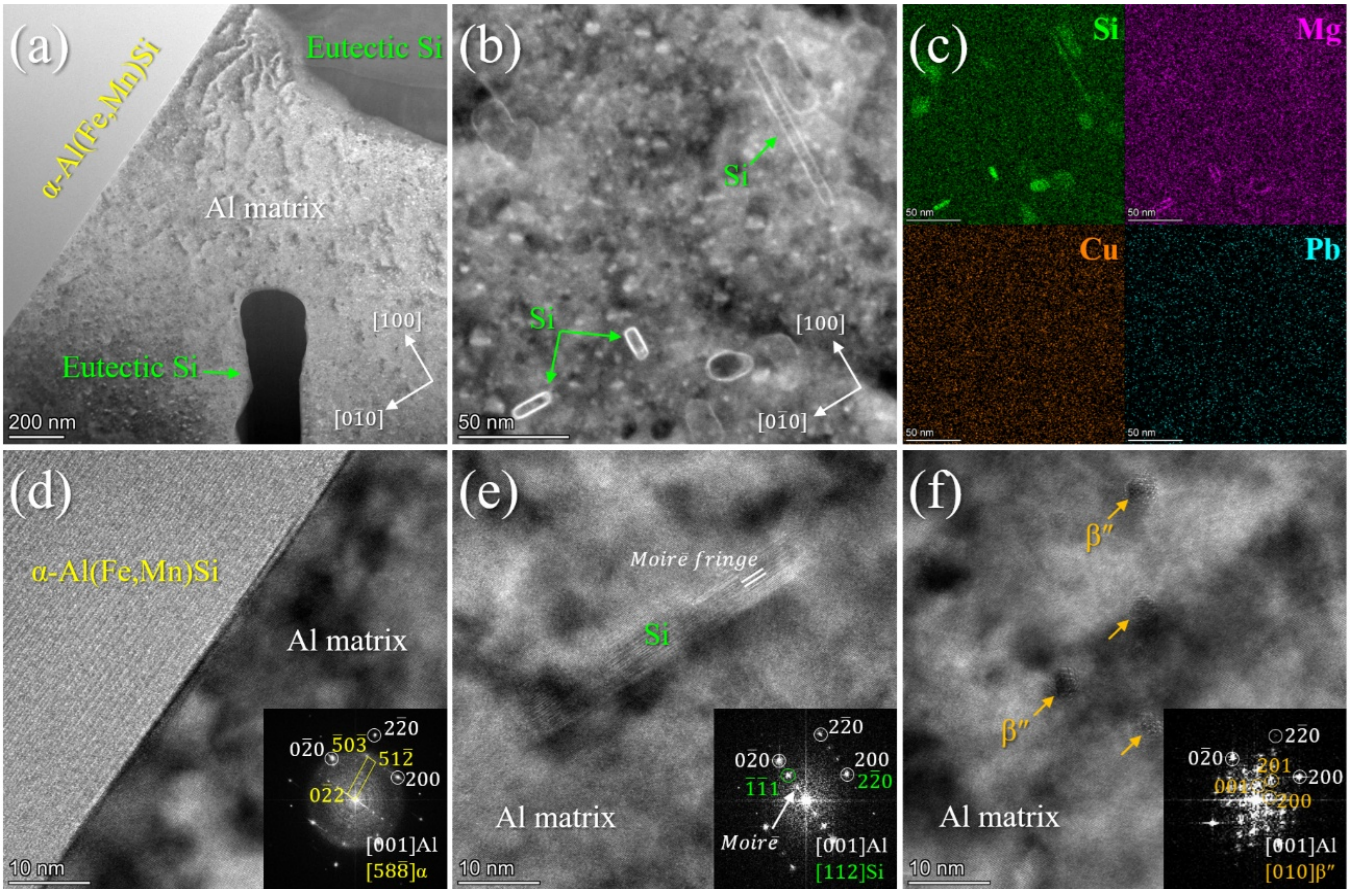


Fig. 3. (a,b) HAADF-STEM images and (c) EDS elemental mapping of the Pb-free alloy aged at 160°C for 8 h. HRTEM and FFT results of (d) $\alpha$-Al(Mn,Fe)Si, (e) Si, and (f) embedded $\beta''$ precipitates

(ORs) of $[001]_{Al}$ // $[58\bar{8}]_{\alpha}$ and $(\bar{2}20)_{Al}$ // $(\bar{5}0\bar{3})_{\alpha}$ (Fig. 3(d)). This $\alpha$-Al(Fe,Mn)Si phase is similarly observed in the Pb-added alloy, indicating that the effect of Pb addition on the formation of primary $\alpha$-Al(Fe,Mn)Si phase is minimal.

Figs. 3(b,c) show HAADF STEM and EDS mapping results revealing the presence of needle-like and spherical Si-rich nanoprecipitates with lengths of 33±17 nm in the Al matrix of the aged Pb-free alloy. The Mg segregation was observed at the interface of the Si nanoprecipitates, which is similarly reported in HPDC A383 Al alloy [19]. Fig. 3(e) shows high-resolution TEM (HRTEM) and fast Fourier transform (FFT) results of needle-like Si nanoprecipitates. The cubic Si precipitates ($Fd\bar{3}m$; $a$ = 0.544 nm [20]) are aligned along ⟨100⟩ directions and have ORs of $[001]_{Al}$ // $[112]_{Si}$ and $(0\bar{2}0)_{Al}$ // $(\bar{1}\,\bar{1}1)_{Si}$. The observed ORs are equivalent to the ORs ($[010]_{Al}$ // $[\bar{1}\,\bar{1}\,\bar{1}]_{Si}$ and $(001)_{Al}$ // $(110)_{Si}$) of the plate or lath-shaped Si nanoprecipitate in an Al–1.3 at.%Si alloy aged at 175°C [21]. Meanwhile, there are fine (<5 nm) nanoprecipitates, which were identified as embedded $\beta''$-$Mg_5Si_6$ precipitates (Fig. 3(f)). The $\beta''$ nanoprecipitates exhibited the ORs of $[010]_{Al}$ // $[010]_{\beta''}$ and $(0\bar{2}0)_{Al}$ // $(\bar{4}03)_{\beta''}$, which is consistent with the ORs reported in Al–0.65Mg–0.73Si–0.13Cu alloy aged at 200°C [22].

Fig. 4(a) shows the HAADF STEM image of Pb-added alloy aged at 160°C for 8 h. As in the Pb-free alloy, needle-like and spherical Si-rich nanoprecipitates (20-40 nm) were observed in the Pb-added alloy. However, a small amount of Pb nanoprecipitates (10-20 nm) were additionally observed in the Pb-added alloy. EDS mapping (Fig. 4(b)) and line scan (Fig. 4(c)) results show that the Pb and Mg elements were segregated at the interface of the Si nanoprecipitates. Pb segregation at the Si precipitate interface is primarily driven by its extremely low solubility in both Si and Al matrix, coupled with the substantial reduction in Si/matrix interfacial energy by Pb segregation [23,24]. HRTEM and FFT analyses confirmed that spherical and needle-like Si nanoprecipitates had different ORs, which are $[001]_{Al}$ // $[100]_{Si}$ and $(200)_{Al}$ // $(011)_{Si}$ for spherical Si (Fig. 4(d)) and $[001]_{Al}$ // $[112]_{Si}$ and $(0\bar{2}0)_{Al}$ // $(\bar{1}\,\bar{1}1)_{Si}$ for needle-like Si (Fig. 4(e)). The embedded $\beta''$ nanoprecipitates (<5 nm) were also present in the aged Pb-added alloy. This indicates that age hardening of Pb-free and Pb-added alloys is due to the Si and $\beta''$ nanoprecipitates, which can act as effective obstacles to dislocation motions.

Interestingly, Pb-added alloy contained Si nanoprecipitates with shorter lengths (33±17 nm) compared to the Pb-free alloy (40±23 nm). This is mainly attributed to the segregation of Pb at the precipitate-matrix interfaces, which can restrict precipitate growth as reported in a Sc/Fe-modified $\theta$' nanoprecipitate [25]. The finer Si nanoprecipitates and Pb nanoprecipitates (Fig. 4(a)) enhance the precipitation strengthening, resulting in the Pb-added alloy exhibiting higher hardness compared to the Pb-free alloy.

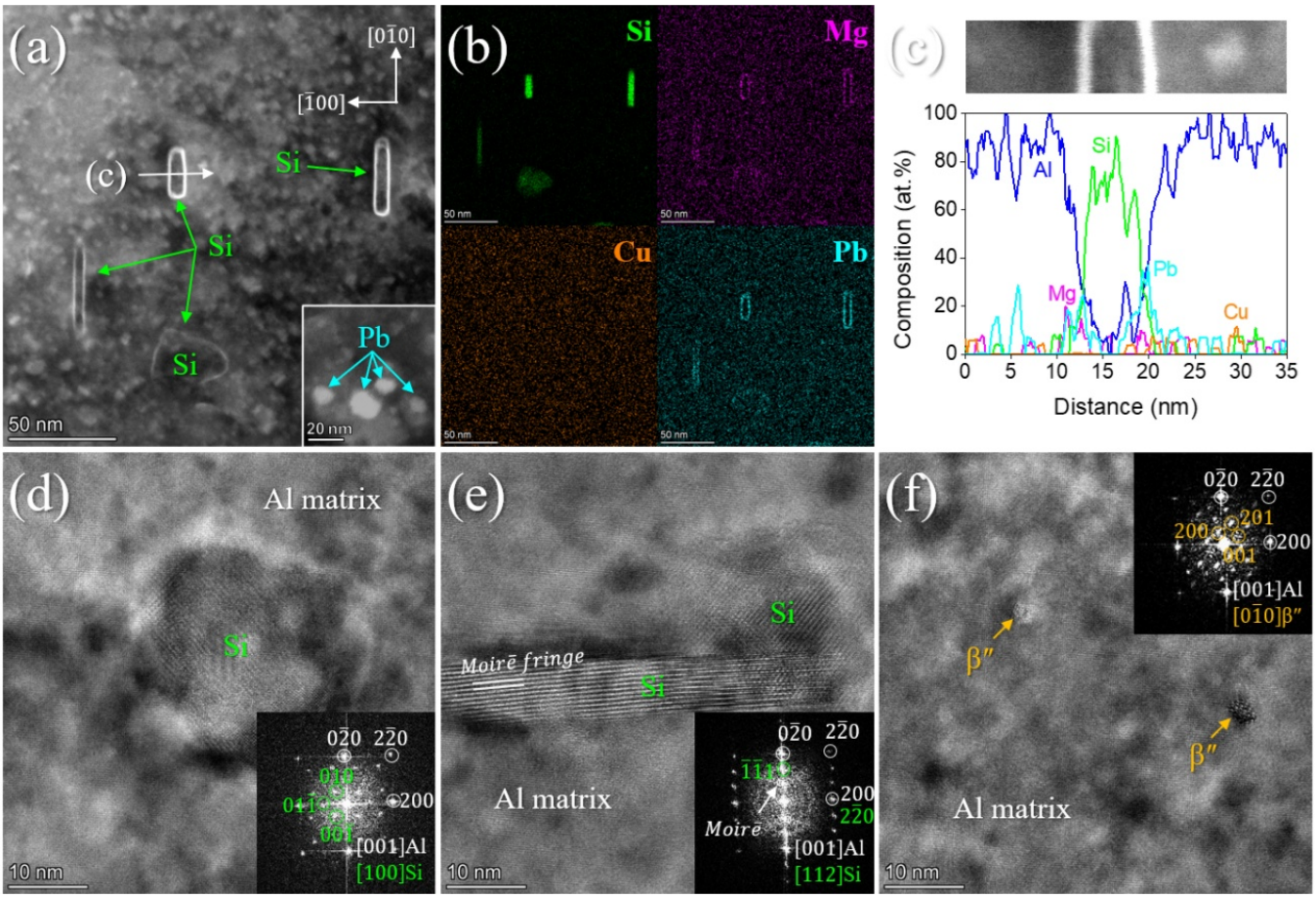


Fig. 4. (a) HAADF-STEM and EDS (b) mapping and (c) line scan results of the Si precipitates of the Pb-added alloy aged at 160°C for 8 h. HRTEM and FFT results of (d,e) Si and (f) embedded $\beta''$ precipitates

Further investigations are underway to elucidate the cause of the different age hardening responses due to Pb addition. This experimental study provides guidelines for the utilization of recycled HPDC Al alloys by demonstrating the beneficial effects of Pb addition on age hardening behavior.

## 4. Conclusions

1) The HPDC alloy consists of coarse dendritic or fine equiaxed Al matrix, Al/Si eutectic, and $\alpha$-Al(Fe,Mn)Si, $\pi$-$Al_8FeMg_3Si_6$, and $\theta$-$Al_2Cu$ phases. The addition of 0.63 wt.%Pb induces the formation of Pb phases along grain boundaries during solidification.
2) Aging at 160°C for 8 h (T5 temper) induces the formation of Si and $\beta''$ nanoprecipitates in both Pb-free and Pb-added alloys. The Si nanoprecipitates exhibit spherical or needle-like morphology with preferred ORs. Mg segregation is observed at the interface of the Si nanoprecipitates for both Pb-free and Pb-added alloys, while additional Pb interfacial segregation exists for the Pb-added alloy. The embedded $\beta''$ nanoprecipitates were observed in both alloys.
3) T5 treatment increases the hardness of Pb-free and Pb-added alloys, mainly due to the precipitation strengthening of Si and $\beta''$ nanoprecipitates. The age hardening response of the Pb-added alloy was slightly higher than that of the Pb-free alloy, due to refinement of Si nanoprecipitates and newly formed Pb nanoprecipitates.

**Acknowledgments**

This work was supported by the Technology Innovation Program (20020283) funded by the Ministry of Trade, Industry & Energy (MOTIE, Korea). It was also supported by the "Research Base Construction Fund Support Program" funded by Jeonbuk National University in 2025. We thank the Center for University-wide Research Facilities (CURF) at Jeonbuk National University for assistance with the experiment.

## REFERENCES

[1] E. Lordan, Y. Zhang, K. Dou, A. Jacot, C. Tzileroglou, P. Blake, Z. Fan, Mater. Sci. Eng. A **817**, 141391 (2021).
[2] H.-W. Son, J.-Y. Lee, Y.-H. Cho, J. Jang, S.-B. Kim, J.-M. Lee, J. Alloys Compd. **960**, 170982 (2023).
[3] B. Zhao, B. Ye, L. Wang, Y. Bai, X. Yu, Q. Wang, W. Yang, Mater. Sci. Eng. A **849**, 143463 (2022).
[4] J. Lee, M. Kang, D. Kim, S.-J. Lee, J.-G. Jung, J. Mater. Res. Technol. **42**, 2310-2318 (2026).
[5] G.S. Peng, X.Y. Fu, Y.C. Gu, G.S. Song, S.S. Chen, Q.Q. Sun, W.D. Hua, J. Mater. Eng. Perform. **31**, 5432-5440 (2022).
[6] S.H. Kayani, S.-U. Lee, K. Euh, J.-M. Lee, Y.-H. Cho, J. Alloys Compd. **976**, 173004 (2024).
[7] S.-H. Lee, N. Seo, M. Kang, S.B. Son, S.-J. Lee, J.-G. Jung, Mater. Charact. **215**, 114204 (2024).
[8] G.K. Sigworth, R.J. Donahue, Inter. Metalcast. **15**, 1031-1046 (2021).
[9] S.K. Das, J.A.S. Green, J.G. Kaufman, JOM **59**, 47-51 (2007).
[10] R. Lin, B. Liu, J. Zhang, S. Zhang, J. Mater. Res. Technol. **19**, 354-367 (2022).
[11] B. Zhou, B. Liu, S. Zhang, R. Lin, Y. Jiang, X. Lan, J. Alloys Compd. **879**, 160407 (2021).
[12] S. Pogatscher, S. Samberger, 2024 IOP Conf. Ser.: Mater. Sci. Eng. **1315**, 012008 (2024).
[13] G. Gaustad, E. Olivetti, R. Kirchain, Resour. Conserv. Recycl. **58**, 79-87 (2012).
[14] S. Shankar, Upcycling Low Quality Automotive Aluminum Scrap, University of California (2025).
[15] L. Pilote, A.E. Gheribi, P. Chartrand, Calphad **61**, 275-287 (2018).
[16] A. Tomar, R. Mittal, D. Singh, Int. J. Miner. Metall. Mater. **21**, 1222-1227 (2014).
[17] C.W. Bale, E. Bélisle, P. Chartrand, S.A. Decterov, G. Eriksson, A.E. Gheribi, K. Hack, I.-H. Jung, Y.-B. Kang, J. Melançon, A.D. Pelton, S. Petersen, C. Robelin, J. Sangster, P. Spencer, M.-A. Van Ende, Calphad **54**, 35-53 (2016).
[18] K. Sugiyama, N. Kaji, K. Hiraga, Acta Crystallogr. C **54**, 445-447 (1998).
[19] T. Liu, Z. Pei, D. Barton, G.B. Thompson, L.N. Brewer, Acta Mater. **224**, 117500 (2022).
[20] E.R. Jette, F. Foote, J. Chem. Phys. **3**, 605-616 (1935).
[21] C.D. Marioara, S.J. Andersen, A. Birkeland, R. Holmestad, J. Mater. Sci. **43**, 4962-4971 (2008).
[22] W. Yang, M. Wang, Y. Jia, R. Zhang, Metall. Mater. Trans. A **42**, 2917-2929 (2011).
[23] L. Pilote, A.E. Gheribi, P. Chartrand, Calphad **61**, 275-287 (2018).
[24] R.W. Olesinski, G.J. Abbaschian, Bull. Alloy Phase Diagrams **5**, 271-273 (1984).
[25] Y.H. Gao, P.F. Guan, R. Su, H.W. Chen, C. Yang, C.He, L.F. Cao, H. Song, J.Y. Zhang, X.F. Zhang, G. Liu, J.F. Nie, J. Sun, E. Ma, Mater. Res. Lett. **8**, 446-453 (2020).